Journal of Volcanology and Geothermal Research 300 (2015) 58–69

Contents lists available at ScienceDirect

Journal of Volcanology and Geothermal Research

journal homepage: www.elsevier.com/locate/jvolgeores

Use of motion estimation algorithms for improved flux measurements using SO_2 cameras

Nial Peters [a,*], Alex Hoffmann [a], Talfan Barnie [b], Michael Herzog [a], Clive Oppenheimer [a]

[a] Department of Geography, University of Cambridge, Downing Place, Cambridge CB2 3EN, UK
[b] Laboratoire Magmas et Volcans, CNRS, IRD, Observatoire de Physique du Globe de Clermont-Ferrand, Université Blaise Pascal, Clermont-Ferrand, France

ARTICLE INFO

Article history:
Received 3 April 2014
Accepted 18 August 2014
Available online 18 September 2014

Keywords:
SO_2 flux
SO_2 camera
Plume speed
Plume modelling
Optical-flow
Motion estimation

ABSTRACT

SO_2 cameras are rapidly gaining popularity as a tool for monitoring SO_2 emissions from volcanoes. Several different SO_2 camera systems have been developed with varying patterns of image acquisition in space, time and wavelength. Despite this diversity, there are two steps common to the workflows of most of these systems; aligning images of different wavelengths to calculate apparent absorbance and estimating plume transport speeds, both of which can be achieved using motion estimation algorithms. Here we present two such algorithms, a Dual Tree Complex Wavelet Transform-based algorithm and the Farnebäck Optical Flow algorithm. We assess their accuracy using a synthetic dataset created using the numeric cloud-resolving model ATHAM, and then apply them to real world data from Villarrica volcano. Both algorithms are found to perform well and the ATHAM simulations offer useful datasets for benchmarking and validating future algorithms.

1. Introduction

SO_2 cameras are the latest addition to the family of UV spectroscopy techniques used to measure sulphur dioxide (SO_2) emissions. Since the first volcanological demonstrations (Mori and Burton, 2006; Bluth et al., 2007) they have been used in numerous studies of SO_2 fluxes from volcanoes (e.g. (Holland et al., 2011; Tamburello et al., 2011; Campion et al., 2012; Smekens et al., 2013; La Spina et al., 2013)). Using SO_2 cameras, estimates of SO_2 flux at ~1 s temporal resolution are possible, enabling studies of highly dynamic degassing events such as Strombolian eruptions (Dalton et al., 2009; Mori and Burton, 2009; Tamburello et al., 2012) and periodic fluctuations in passive degassing (Tamburello et al., 2013; Pering et al., 2014).

SO_2 cameras use bandpass filters to image at two narrow wavebands, one within and one outside-of an absorption band of SO_2 (typically centred at 310 and 330 nm, respectively). The cameras operate on the principle that the apparent absorbance between the two bands will vary only as a function of atmospheric species that absorb unequally across them (Mori and Burton, 2006). However, the calibration of apparent absorbance to SO_2 column amount is non-trivial (Kantzas et al., 2010; Kern et al., 2010, 2013; Lübcke et al., 2012).

Images at the two wavebands are either captured simultaneously, necessitating two separate cameras, or sequentially, using a filter wheel to change the recorded waveband for each image. The latter method permits a single camera unit to be used, but at the expense of having a short time delay between the two images. Since volcanic plumes are seldom stationary in the atmosphere, this is clearly undesirable. Heterogeneities may have shifted by several pixels between consecutive images, compromising the SO_2 retrieval method described above. The simultaneous capture of images at two wavebands is also problematic, since the retrieval of SO_2 column amounts requires single-pixel correspondence between the two images. When SO_2 cameras are used "in the field" they are often subjected to rapid temperature changes, vibration and physical shocks. Alignment of optical components to the degree of single-pixel correspondence is simply not practical. Relative offset and rotation between the image planes of the two cameras will lead to different fields of view and differing parallax effects. Although parallax effects become negligible at large distances, it is not uncommon for SO_2 cameras to be used at close range to volcanic plumes. In addition, the two lenses may exhibit different distortion effects due to their different filters, manufacturing defects and differences in focus and aperture settings. Individually these effects may be small to negligible, but they compound each other to produce an offset that results in "fringing" around contrast boundaries in the apparent absorbance image, where the misalignment results in high and low valued pixels being ratioed with each other. This leads to spurious high and low values of SO_2 column amount in the calibrated images, which might inhibit subjective interpretation and introduce significant error in integrating over small plumes to find total mass.

A further problem, also applicable to other gas flux measurement techniques (e.g. (McGonigle et al., 2005b)), is that of estimating plume transport speed. To calculate flux from SO_2 camera images,

* Corresponding author.
E-mail address: njp39@cam.ac.uk (N. Peters).

http://dx.doi.org/10.1016/j.jvolgeores.2014.08.031
0377-0273/

the SO_2 column amounts must be integrated across a transect of the plume and multiplied by the transport speed perpendicular to the transect. Typically, the plume speed is found by cross-correlating the integrated column amount values from two complete transects of the plume at different distances from the vent (McGonigle et al., 2005a; Mori and Burton, 2006; Williams-Jones et al., 2006). This method assumes a uniform velocity field across the entire plume and does not account for complex flow structures or vorticity. (Boichu et al., 2010) discuss in more detail the compromises that must be made between time- and motion-resolution when using the cross-correlation method.

Estimating plume speed and accurate registration of images from two separate cameras are essentially the same problem; that of calculating motion vectors which map pixels in one image to their corresponding positions in another. This is a common computer-vision problem, which is addressed by a large number of well-established motion estimation algorithms of varying complexity and trade-offs (e.g. Geiger et al., 2014). To date, use of these techniques in volcanology has mostly been constrained to estimating lava motion from infrared images (James et al., 2007; Oppenheimer et al., 2009; Lev et al., 2012; Peters et al., 2014a), and their application to SO_2 camera images has so far been limited to the work (Kern et al., 2012) who demonstrated how optical-flow methods may be used to estimate SO_2 flux. We extend this work here by assessing the performance of two different motion estimation algorithms when applied to SO_2 camera images, both for flux estimation and for registering images from separate cameras. We use both a Dual-Tree Complex Wavelet Transform (DT-ℂWT) algorithm (Magarey and Kingsbury, 1998), and the Farnebäck optical-flow algorithm (Farnebäck, 2003).

As already discussed, a major problem with estimating plume transport speeds is that of validation. With little possibility of accurately measuring plume speed by an alternative method, it is difficult to assess the performance of the techniques being developed to estimate plume speeds and to constrain the errors which they may introduce. In an attempt to address this issue, we use the Active Tracer High-Resolution Atmospheric Model (ATHAM) (Oberhuber et al., 1998; Herzog et al., 2003) run in a two-dimensional configuration to create a set of synthetic images of a volcanic plume from a passively degassing volcano. Algorithms for estimating plume speed can be applied to the synthetic images and the results compared to the "real" velocity field computed by the model, providing a simple method of assessing their performance in the context of volcanic plume observations. We demonstrate the technique with both the DT-ℂWT and Farnebäck motion estimation algorithms.

It is not our intent to conduct an in-depth comparison of the many different motion estimation algorithms available, and we acknowledge that more suitable algorithms may exist for use with SO_2 camera images than the two which we present here. Instead, we hope to demonstrate the potential applications and benefits of motion estimation algorithms in volcanic-plume imaging, and establish a framework for validating and comparing them within this context.

Our specific aims are threefold: (i) to present two different motion estimation algorithms which are suitable for use with images from SO_2 cameras and show how they perform on both real and synthetic data, (ii) to introduce the ATHAM model as a tool for validating plume transport speed estimation methods, (iii) to demonstrate how these algorithms can be employed to provide accurate registration of images from separate camera units.

2. Methodology

2.1. Motion estimation algorithms

The DT-ℂWT algorithm works by decomposing images using the Dual-Tree Complex Wavelet Transform (Kingsbury, 2001). The phase shift between the decomposed subimages of two frames is related to the motion of features between those frames. The algorithm employs an iterative approach, using coarse features to create an initial motion estimate and then refining this using progressively finer-scale features. Full details of the algorithm are given by (Magarey and Kingsbury, 1998).

The DT-ℂWT algorithm has been used in previous volcanological studies to estimate the surface motion of the lava lake at Erebus volcano from time series of infrared images (Oppenheimer et al., 2009; Peters et al., 2014b). Whilst this is clearly a very different scenario to that of estimating plume transport speeds from SO_2 camera images, many of the fundamental problems are the same; identifiable features are often diffuse, transient, and may change significantly between frames. The algorithm copes well under these conditions, and is also robust against the noise introduced by varying amounts of volcanic plume, which degrades the camera's view of the lake.

The Farnebäck algorithm works by expressing the local neighbourhoods of each pixel in the images as polynomial expansions. The translations between the polynomial expansions for each successive frame can then be calculated and, by enforcing a certain model of motion (e.g. the affine motion model) the two-dimensional displacement field can be estimated. The Farnebäck algorithm also employs an iterative approach, with a starting estimate for motion being derived from coarse features and then refined using progressively finer features. The algorithm is described in detail by (Farnebäck, 2003).

In this investigation we used the same implementation of the DT-ℂWT algorithm as (Oppenheimer et al., 2009; Peters et al., 2014a). MatLab code for this was kindly provided by Prof. Nick Kingsbury at the Engineering Department of the University of Cambridge. We used the implementation of the Farnebäck algorithm provided by the open-source computer-vision library OpenCV (Bradski, 2000).

Both of these implementations allow several parameters to be set by the user to control the operation of the algorithm. A description of the parameters along with the specific values used for this study is given in Appendix A. Broadly speaking the parameters set both the averaging level and the scale of features used by the algorithms. Selecting higher averaging and larger features will usually result in a more robust (less prone to noise, more tolerant of transient features) motion estimate, but at the expense of a less detailed motion field.

2.2. Using ATHAM as a validation tool

We used the non-hydrostatic, fully compressible, multiphase, mesoscale Active Tracer High-Resolution Atmospheric Model (ATHAM) to simulate a synthetic SO_2 plume from passive degassing of an idealised volcano, loosely based on Villarrica volcano, Chile. Built within the Large Eddy Simulation framework, ATHAM was originally designed for simulating plinian eruption dynamics (Herzog et al., 1998, 2003; Oberhuber et al., 1998). It has also been used for research into volcanic gas scavenging, particle aggregation and interactions with microphysics (Textor et al., 2006a,b), and more recently, into the dynamics of large co-ignimbrite (Herzog and Graf, 2010) and phreatomagmatic (Van Eaton et al., 2012) eruption clouds.

ATHAM is based on a modular structure that facilitates the coupling of specific process modules to the dynamical core. The core solves, within an Eulerian framework, the Navier–Stokes equations of momentum, and the pressure, temperature and tracer transport equations for a gas-particle mixture (Oberhuber et al., 1998). Active tracers, i.e. solid, liquid or gaseous components that have their own heat capacities and densities, influence the mixture's flow by changing its thermodynamic and dynamic properties. Momentum and tracer equations are described in flux form to guarantee conservation of momentum and mass; the heat transport equation is in advective form.

Short- and longwave radiative transfer, as well as surface fluxes of sensible and latent heat, have not been applied in our model runs, to reduce complexity and computational expense. Resolved and unresolved turbulent entrainment of ambient air into the plume modifies its

buoyancy and disperses tracers and temperature anomalies. Subgrid-scale (SGS) turbulence is treated as eddy diffusivity and parametrised on the basis of a 1.5-order prognostic SGS anisotropic turbulent kinetic energy (TKE) closure scheme, described by (Herzog et al., 2003). The mixed-phase cloud microphysics included in the model correspond to a simple prognostic bulk Kessler-type approach, predicting cloud droplets, rain, ice crystals and graupel as specific concentrations (Herzog et al., 1998). The current model configuration does not include aerosol microphysics and nucleation, cloud nuclei activation, or ash aggregation. The configuration of ATHAM used in this study is described in detail in Appendix B.

The model output was used to create a set of synthetic calibrated SO_2 camera images, where pixel values represent column amounts of SO_2 in kg m^{-2}. The motion estimation algorithms were then applied to these images, and their performance evaluated by comparing the calculated SO_2 flux across a particular line of pixels to its real value (calculated using the motion field from the model output). The fluxes were calculated by integrating the product of the SO_2 column amounts across a transect of the image with the components of the velocity perpendicular to that transect.

Prior to applying the motion estimation algorithms, background and foreground regions (i.e. clear sky and the ground) were masked with Gaussian-distributed white noise, with a mean value approximating that of the pixels within the plume. This was found to greatly improve the performance of both algorithms, preventing spurious motion vectors from being computed in regions of very little texture and at high contrast boundaries.

2.3. Villarrica dataset

A ~20 min sequence of SO_2 camera images recorded at Villarrica volcano, Chile, on 8 February 2012 was used to test both algorithms' performance on "real" data. The images were captured using an Apogee Alta U47-SO_2 camera with an E2V CCD47-10, 1024 × 1024 pixel CCD and fitted with a 50 mm lens, giving a single pixel "footprint" of 1.04 m^2 (distance to the plume was approximately 4 km). The camera used a filter-wheel to alternate between recording images with and without SO_2 absorbance. The images were calibrated into SO_2 column amounts using a co-located UV spectrometer, following the methodology of Lübcke et al. (2012). Images were recorded every 4 s.

As in the case of the ATHAM data, random noise was used to mask background and foreground regions prior to motion estimation. It should be noted however, that as some background regions of the image reach SO_2 amounts greater than the background threshold, anomalous motion vectors may be produced (see for example Video 5 and Video 6 in the supplementary materials). This does not have a significant effect on the flux calculations since the amount of SO_2 associated with these motion vectors is very small.

2.4. Image registration

As already discussed, there are numerous factors that can contribute to geometric distortion between the images at different wavebands in a two-camera system, and correcting for this is important in order to prevent "fringing" in the calibrated images. To demonstrate how motion estimation algorithms may be used to ensure an accurate mapping between pixels from different cameras (i.e. between the images with and without SO_2 absorbance), we used a single SO_2 camera image of Villarrica and applied a known distortion to it using OpenCV's *cvWarpImage* function (described in detail by (Bradski and Kaehler, 2008)). As shown in Fig. 1, the distortion was made up of a perspective shift (the expected effect if the optical planes of the two cameras are not co-planar), and a rotation of 0.5° clockwise about the top left corner of the image. The two motion tracking algorithms were then used to calculate the shift vectors that mapped features in the distorted image to their respective positions in the original image.

In order to distribute errors in the shift estimates across the whole of the corrected image, we used the shift vectors to calculate a single corrective transform which we then applied to the whole image. In this case we assumed a projective distortion, and were therefore able to calculate the optimal (least-squares error) correction using OpenCV's *cvFindHomography* function (described in detail by (Bradski and Kaehler, 2008)). However, more complex corrections (e.g. including lens distortion) could be calculated in a similar manner using the correspondences found by the motion tracking algorithms.

To avoid errors caused by edge effects, we only included shifts from within a set region of interest (ROI) when calculating the corrective transformation. The ROI was selected so as to exclude the edges of the image, the crater region (which has very high intensity contrasts) and the clear sky regions (which have almost no intensity contrast) since motion estimates in these regions are often inaccurate. This selection procedure could potentially be automated by thresholding the image based on texture i.e. excluding regions where variation in pixel value is very small.

3. Results

Fig. 2 shows the results of applying the motion estimation algorithms to the synthetic images produced using ATHAM. Animations showing the velocity fields produced for the full time series of images using the DT-ℂWT (Video 1) and the Farnebäck (Video 2) algorithms are provided in the supplementary material to the online version of this article. The SO_2 fluxes through a horizontal line of pixels 170 m above the crater, calculated using the velocities from ATHAM and the two motion estimation algorithms, are plotted against time. As shown in Fig. 3, the agreement of the estimated fluxes with the fluxes computed from ATHAM is striking and provides a strong argument for the use of

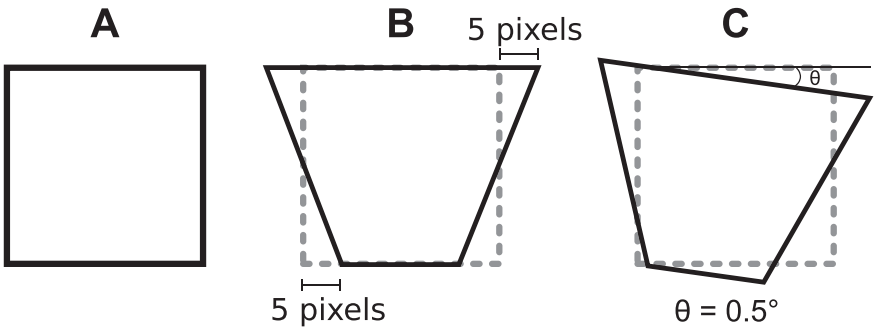

Fig. 1. Cartoon of the distortion used to create a test image for the image registration technique. (A) The original (square) image, (B) perspective shift, (C) rotation (0.5° clockwise about top left corner).

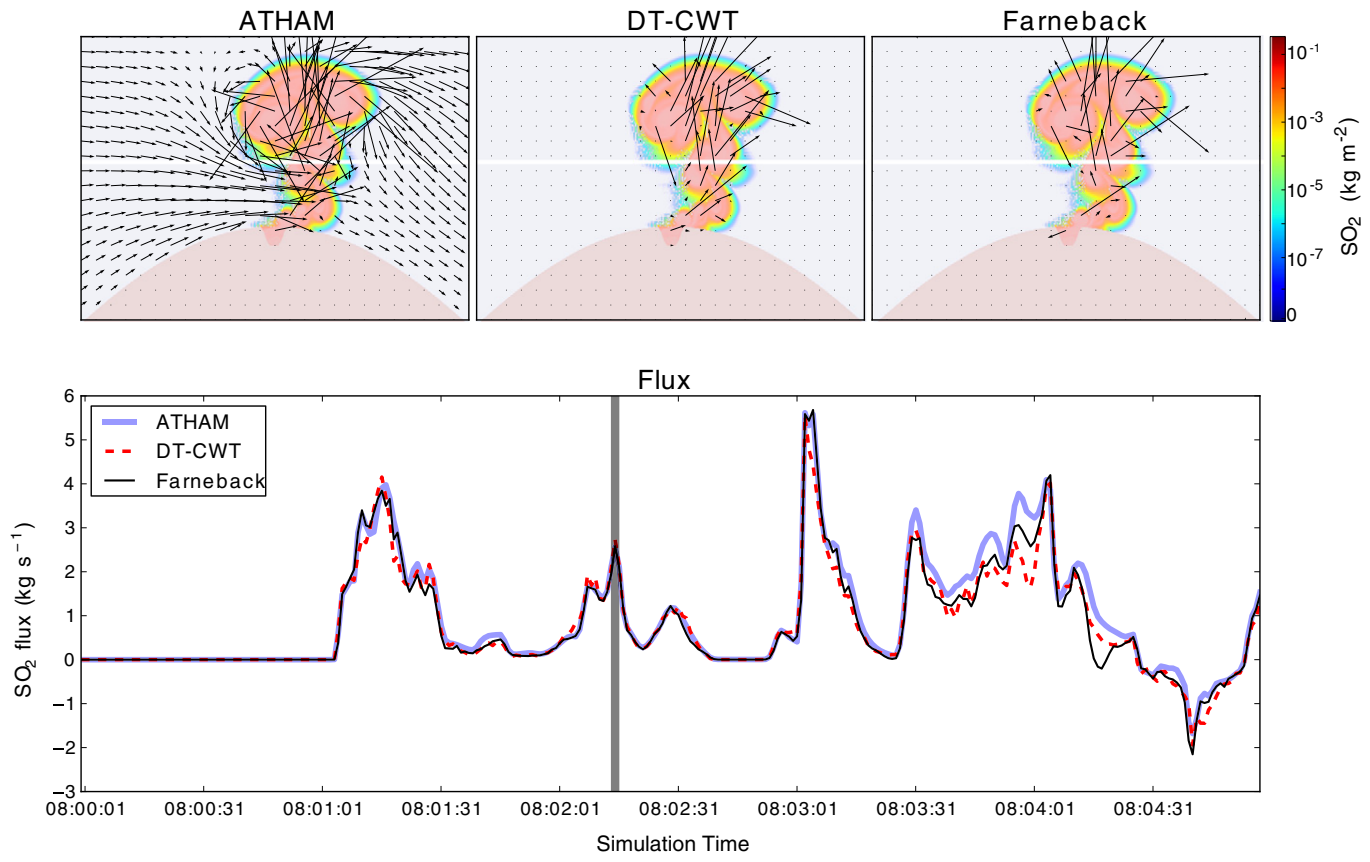

Fig. 2. Summary of results from the "closed-top" ATHAM simulation. SO_2 fluxes calculated using the velocity fields from ATHAM, the DT-ℂWT algorithm, and the Farnebäck algorithm are plotted against time. Snapshots of the velocity fields (corresponding to the time denoted by the vertical grey line) superimposed over the SO_2 amounts are also shown. The line of pixels over which the fluxes were calculated is highlighted in white.

these algorithms in computing plume transport speeds. Both the DT-ℂWT and Farnebäck methods show a good correlation across the full range of flux values, with R^2 values of 0.95 and 0.97 respectively.

It should be noted that the anomalous motion vectors that are occasionally apparent in Video 1 are due to edge effects. Close to the boundaries of an image, strong features that exist in one frame may have disappeared in the next (because they have moved out of the field of view). This causes anomalous motion estimates. This is a common problem with motion estimation algorithms and is not a draw-back of the DT-ℂWT algorithm in particular.

The model used to produce the images for Fig. 2 had a closed top (rigid lid) boundary (as described in Section 2.2), acting essentially in

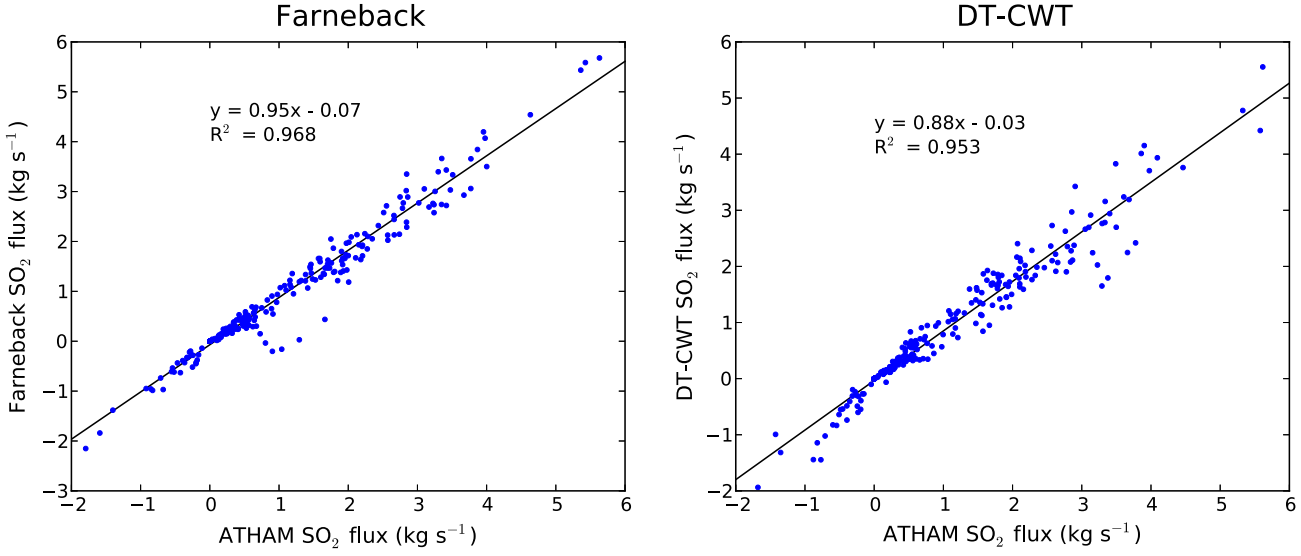

Fig. 3. Scatter plots showing the relationship between the SO_2 fluxes computed using velocity estimates from the Farnebäck (left) and DT-ℂWT (right) algorithms and the real fluxes from the "closed-top" ATHAM model. A linear regression line and the associated R^2 value are also shown.

a similar way as a very strong temperature inversion layer. When the buoyant plume reached the top boundary of the domain, it was forced to spread laterally and large down-welling regions quickly led to a negative flux across the integration line (as can be seen beyond 08:04:31 in Fig. 2). To overcome this issue, an additional 49 vertical grid-points were added, extending the vertical model domain to a total elevation of more than 6 km on a stretched grid. In addition, we increased vertical wind shear by applying a linear multiplier function to the wind profile, varying between 1 and 1.5 over the lower 1.5 km vertical extent of the model domain. Furthermore, we applied ± 20% random white noise onto the initial horizontally homogeneous wind field, and initialised the SGS TKE with isotropic turbulence on the order of 1 $m^2 s^{-2}$, to promote resolved turbulent effects. However, the increased randomisation of the initial conditions did not produce a visibly distinguishable effect in terms of increasing turbulent diffusion, and the resulting streamer-like structural features are characteristic of a 2D model setup. A preliminary analysis of turbulent power spectra as a function of time (not shown) is inconclusive with respect to the influence of this heterogeneous initialization, but the initially high energy at the higher wavenumbers (smaller scales) quickly dissipates over time, and the spectra gradually adopt shapes more alike those with a laminar horizontal flow initialization. This may suggest that the small-scale flow heterogeneities quickly get smoothed out, and that an upscale transport of turbulent kinetic energy cannot be simply induced with grid-point-scale white noise. The formulation of the model's lateral boundary conditions, however, may also have played a role in the reduction of the high wavenumber noise over time.

The motion of the plume produced by this setup was predominantly horizontal (and often grounded in the vicinity of the crater), necessitating a vertical integration line. The results from this simulation are shown in Fig. 4. Note however, that the extended vertical extent of the model domain has been cropped from the plotted data such that the plotted extent matches that of Fig. 2. Once again, the effectiveness of the motion estimation algorithms is clearly demonstrated (Fig. 5). As shown in the animated sequences (Video 3 and Video 4 — see supplementary materials), the periods in which the motion estimation algorithms significantly underestimate the SO_2 flux (e.g. 08:06) correspond to periods when large portions of the plume are grounded at the integration line and lack any significant structure.

Using the same images as for Figs. 2 and 4, we made flux estimates using the conventional cross-correlation technique often used in SO_2 camera imaging (McGonigle et al., 2005a; Mori and Burton, 2006; Williams-Jones et al., 2006). The transects for the cross-correlation were taken from 20 m (10 grid points) either side of the integration lines used in Figs. 2 and 4. Short time series of the resulting fluxes are shown in Figs. 6 and 7. Fig. 6 shows a period when the cross-correlation method performs well, and Fig. 7 shows a period when it does not. Fluxes calculated using velocity estimates from the Farnebäck algorithm are also shown for comparison. It can be seen that although the cross-correlation method produces reasonable flux estimates when the plume consists of discrete puffs (Fig. 6), when the plume is less structured it can produce errors of up to 300% (Fig. 7). The Farnebäck algorithm performs consistently better than the cross-correlation method, and appears to be less sensitive to plume conditions.

As already discussed, it is not possible to quantitatively assess the performance of motion estimation algorithms on real SO_2 camera images. However, some insight can be gained through a visual inspection of the motion vectors produced by the algorithms. Fig. 8 shows a snapshot of the motion vectors calculated by both the DT-ℂWT and Farnebäck algorithms when applied to a sequence of SO_2 camera images

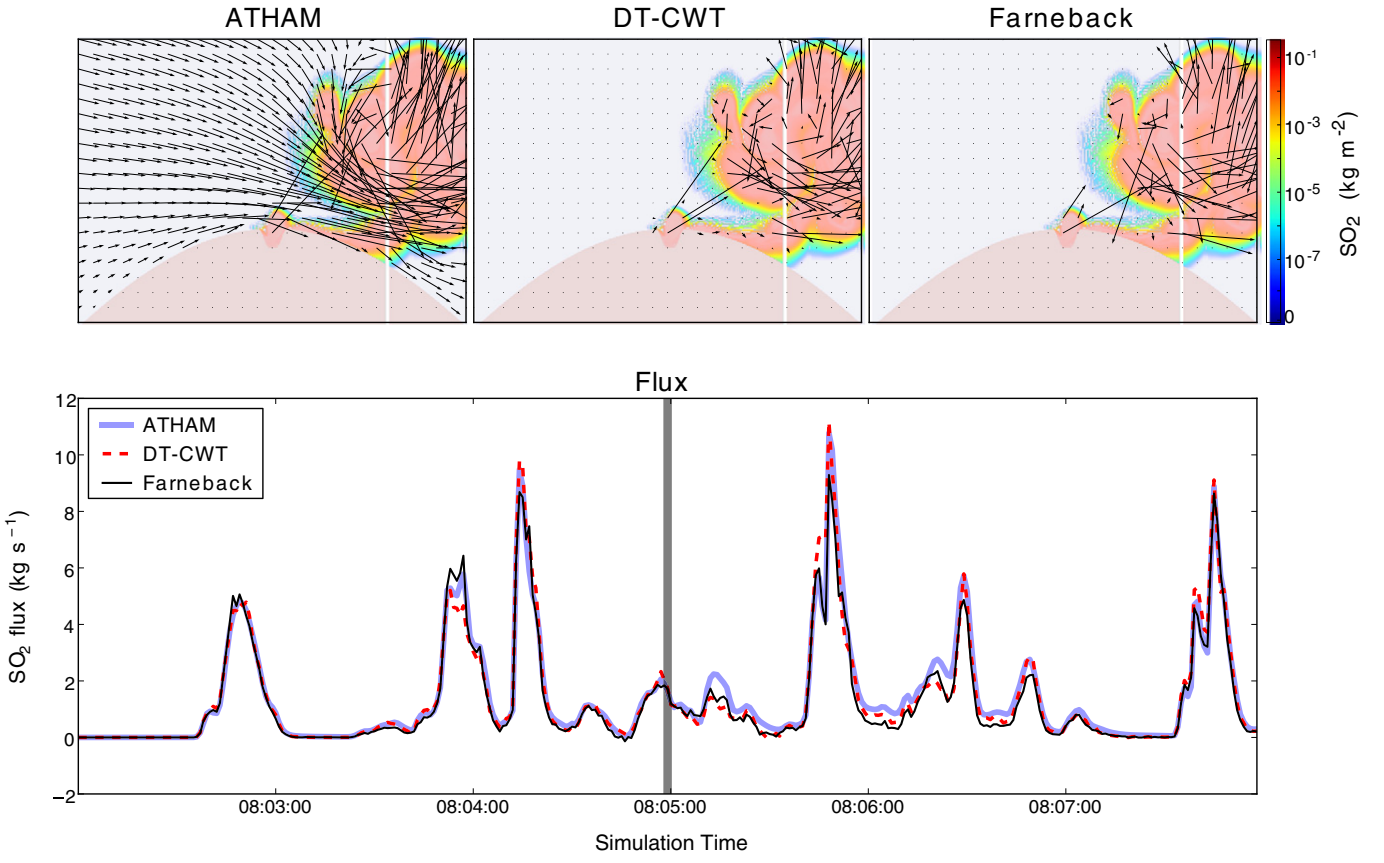

Fig. 4. Summary of results from the "open-top" ATHAM simulation. SO_2 fluxes calculated using the velocity fields from ATHAM, the DT-ℂWT algorithm, and the Farnebäck algorithm are plotted against time. Snapshots of the velocity fields (corresponding to the time denoted by the vertical grey line) superimposed over the SO_2 amounts are also shown. The line of pixels over which the fluxes were calculated is highlighted in white.

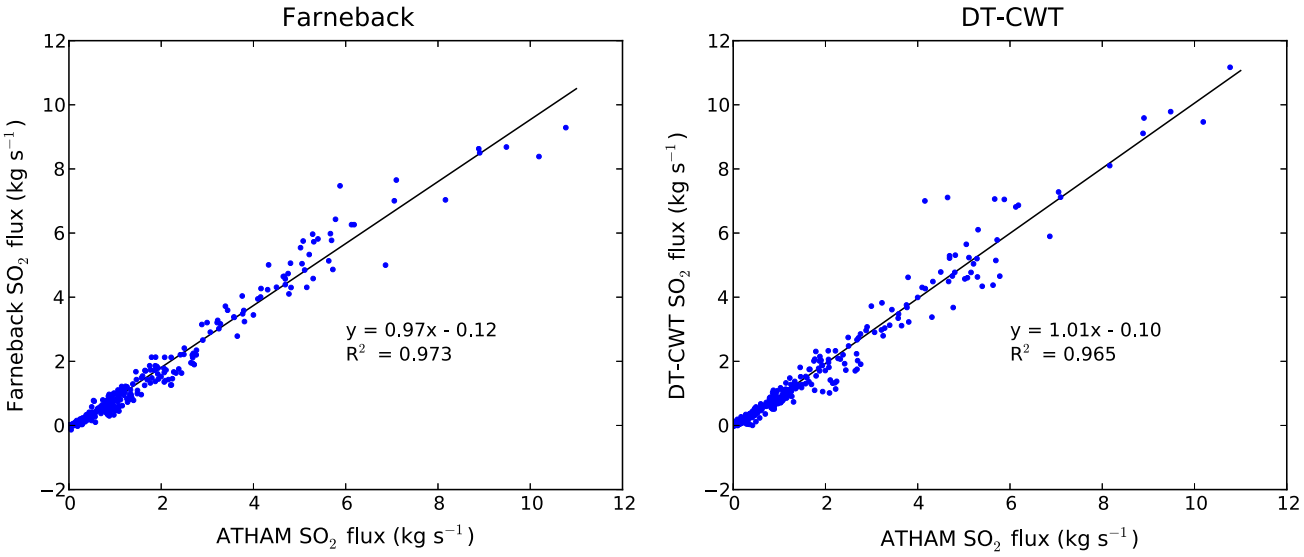

Fig. 5. Scatter plots showing the relationship between the SO_2 fluxes computed using velocity estimates from the Farnebäck (left) and DT-ℂWT (right) algorithms and the real fluxes from the "open-top" ATHAM model. A linear regression line and the associated R^2 value are also shown.

of Villarrica (see Section 2.3). Animations of the motion estimates from the full sequence of images for the DT-ℂWT (Video 5) and the Farnebäck (Video 6) algorithms are provided in the supplementary material to the online version of this article. Both algorithms produce a similar distribution of velocity vectors over the plume region. In general the DT-ℂWT technique produces a smoother velocity field. However, this is likely due to our choice of algorithm parameters rather than a fundamental difference between the algorithms themselves (for example a slightly higher level of averaging). Both algorithms produce a mean plume velocity of around 3.5 m s^{-1}, which seems plausible for Villarrica. Closer inspection of the estimated motion shows, as demonstrated by Fig. 9, that the magnitudes and directions of the velocity vectors from both algorithms match the motion of easily observable features.

Fig. 10B shows a comparison of SO_2 fluxes calculated for the Villarrica data set using the DT-ℂWT algorithm, the Farnebäck algorithm and the cross-correlation technique. The transect lines used are shown in Fig. 10A. The fluxes computed using the DT-ℂWT and Farnebäck algorithms are comparable, and the differences between them are of the same order as when they were applied to the ATHAM data (Figs. 2 and 4). The discrepancy with the cross-correlation method is striking, with cross-correlation consistently giving flux estimates 1.5–2 times higher than the DT-ℂWT and Farnebäck algorithms. Whilst it is not possible to confirm definitively that the cross-correlation method is over-estimating, the DT-ℂWT and Farnebäck fluxes are more in line with previous SO_2 fluxes recorded at Villarrica (Mather et al., 2004a,b; Witter et al., 2004; Shinohara and Witter, 2005; Sawyer et al., 2011). Furthermore, since the cross-correlation method was shown to over-estimate the fluxes for the ATHAM data (Figs. 6 and 7) it seems reasonable to assume that it also over-estimates for real data.

The results of using the DT-ℂWT and Farnebäck algorithms to calculate the corrective transform for a distorted image (as described in Section 2.4) are shown in Fig. 11. To assess the performance of the registration we have plotted the percentage error of each pixel value in the corrected image with respect to its value in the original image, i.e. the error associated with the pixel at coordinates (i, j), $E_{i,j}$, is given by:

$$E_{i,j} = \frac{\left|O_{i,j} - C_{i,j}\right|}{O_{i,j}} \times 100 \quad (1)$$

where $O_{i,j}$ is the pixel value in the original image, and $C_{i,j}$ is its value in the corrected image.

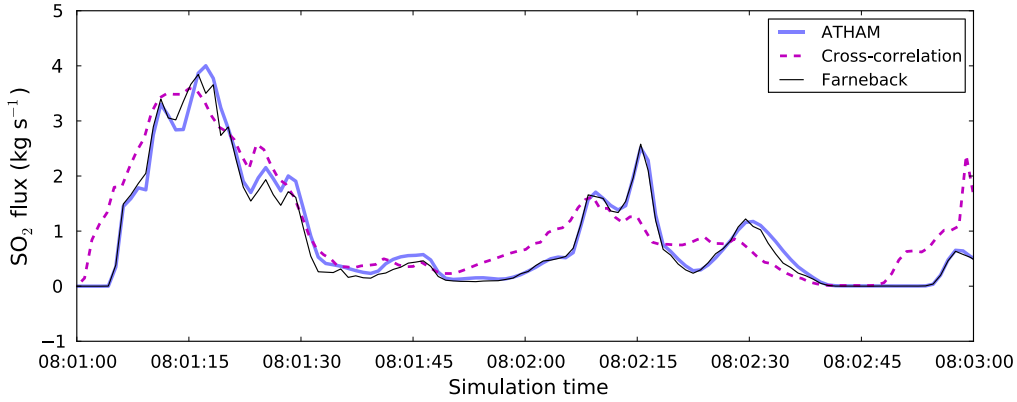

Fig. 6. Short time series comparing SO_2 fluxes calculated from synthetic images from the "closed-top" ATHAM simulation using a simple cross-correlation method and the Farnebäck algorithm. The true fluxes (calculated using the ATHAM velocity field) are also shown. This time period was chosen deliberately as an example of good performance of the cross-correlation technique.

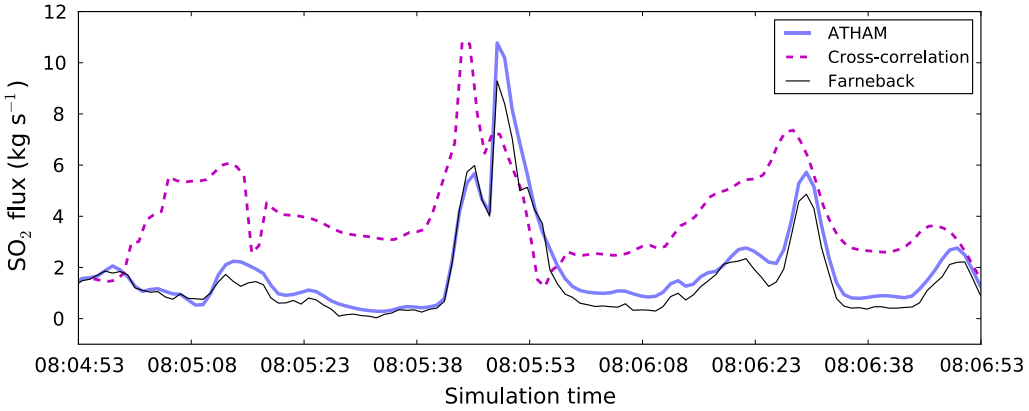

Fig. 7. Short time series comparing SO_2 fluxes calculated from synthetic images from the "open-top" ATHAM simulation using a simple cross-correlation method and the Farnebäck algorithm. The true fluxes (calculated using the ATHAM velocity field) are also shown. This time period was chosen deliberately as an example of poor performance of the cross-correlation technique.

The correction to the image was applied using OpenCV's *cvWarpImage* function (Bradski and Kaehler, 2008) (as was the original distortion). It should be noted that distortion and subsequent correction, even when the transformation is known exactly, leads to errors of 30–40% in the out-of-plume region of the corrected image (where the pixel values are close to zero). This is due to the interpolation required when performing the transformations. The striped pattern observed in the error plots is caused by a small-amplitude periodic fluctuation in the intensities of pixels in the original image, and are not an artefact of the registration technique. We are unclear on the exact origin of this phenomenon but suggest that it may be caused by an instrumental effect due to the particular hardware configuration of the camera. As can be seen in the figure, both algorithms produce similar results, with resultant errors being within the interpolation error of the *cvWarpImage* function. In the plume region, the errors in the corrected images are < 3% for both algorithms.

4. Discussion

In general both algorithms performed similarly, with equal resultant errors when used for image registration, and comparable correlations with real flux values when applied to our synthetic data (Figs. 3 and 5). As previously mentioned, a wide range of motion estimation algorithms exist (e.g. (Geiger et al., 2014)) and it is not our intent to promote

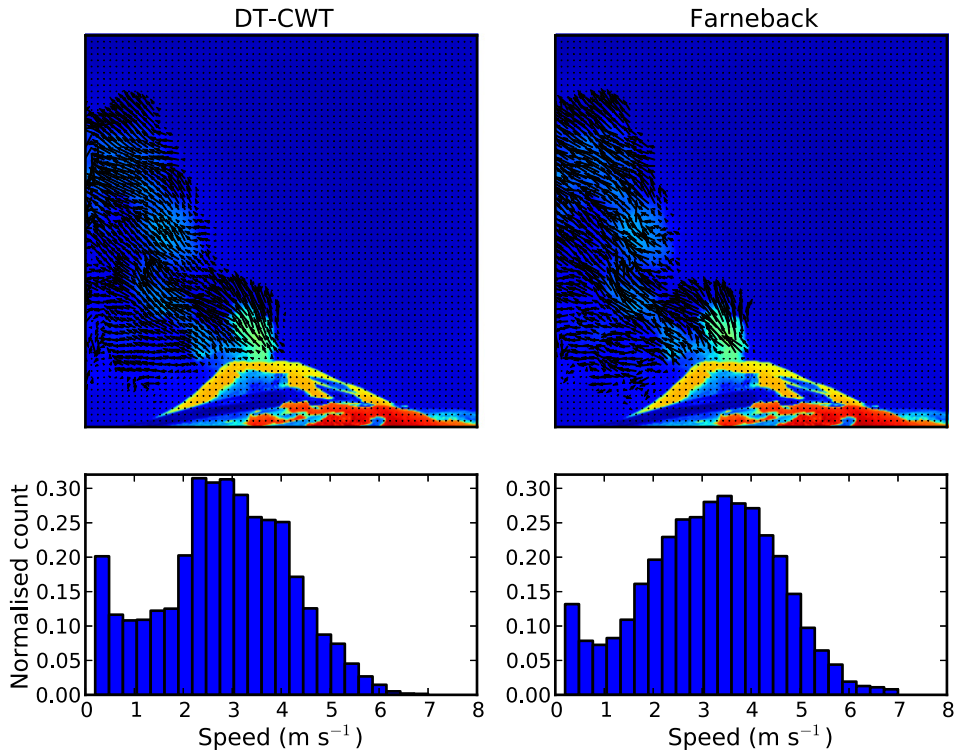

Fig. 8. An SO_2 camera image of Villarrica captured on 8 February 2012 using a 310 nm bandpass filter, with motion vectors estimated using the DT-CWT algorithm (left image) and the Farnebäck algorithm (right image). The images have not been calibrated, and the colour scale is arbitrary. Normalised histograms showing the distribution of magnitudes of the velocity vectors produced by each method are also plotted. Motion vectors from the outside 10 pixels of the image have been excluded from the histograms, as have the zero velocity vectors.

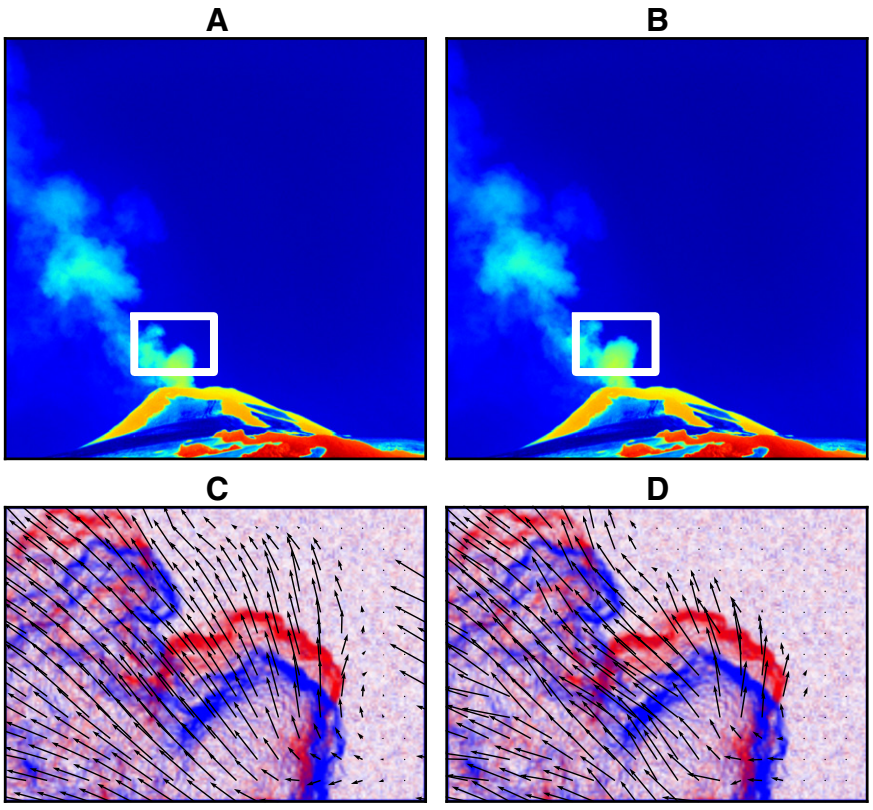

Fig. 9. (A, B) Two successive SO_2 camera images (using a 310 nm bandpass filter) of Villarrica with a ~4 s delay between them, the region displayed in C and D is denoted by the white rectangles. The images have not been calibrated, and the colour scale is arbitrary. (C, D) Motion vectors mapping pixels in A to their corresponding positions in B; computed using the DT-ℂWT algorithm (C) and the Farnebäck algorithm (D). Notable features in the plume from image A (blue) and B (red) have been enhanced using Sobel edge detection and are displayed. Correct motion vectors are expected to point from features shown in blue to the corresponding feature in red.

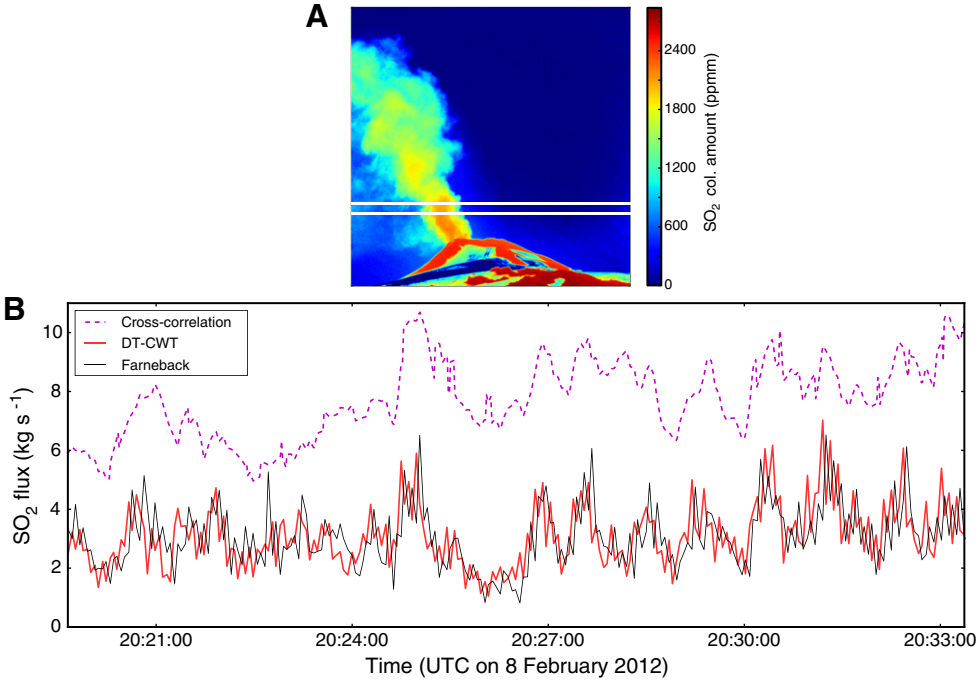

Fig. 10. (A) Calibrated SO_2 camera image of Villarrica. The transects used for the cross-correlation are shown in white. The lower of these was used as the integration line for three flux estimates. (B) Time series of SO_2 fluxes from Villarrica on 8 February 2012 calculated using plume speeds from the cross-correlation method, the DT-ℂWT algorithm and the Farnebäck algorithm.

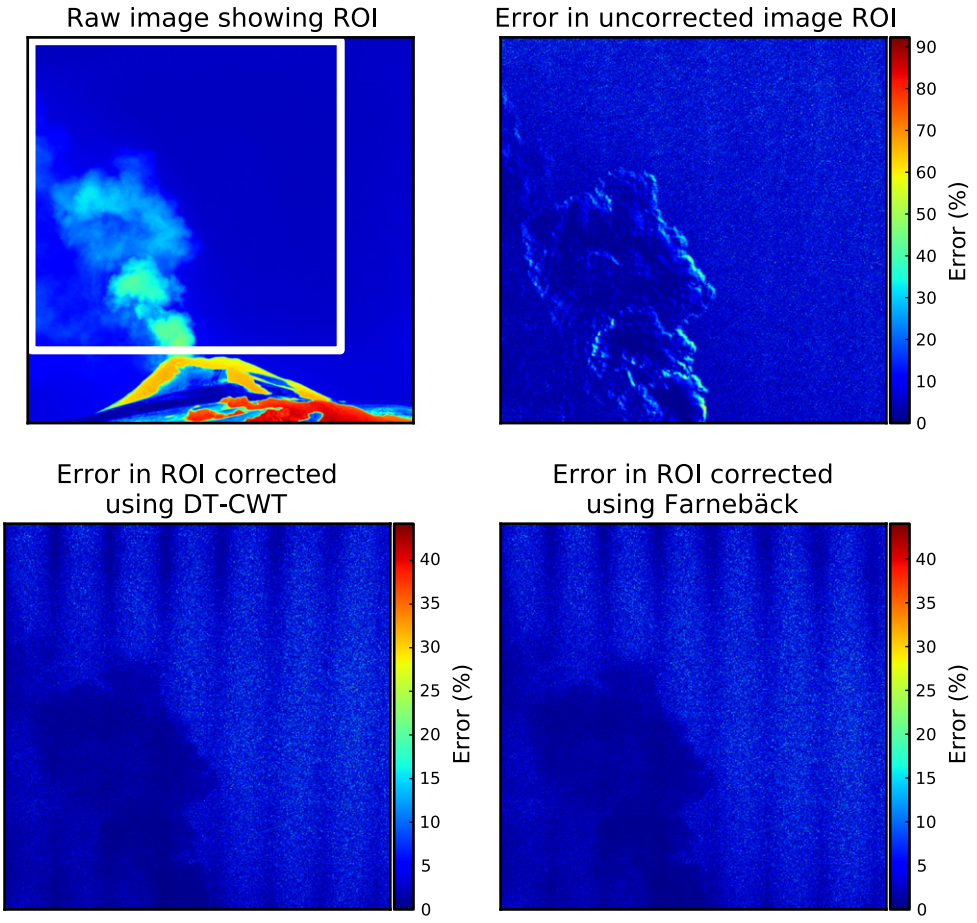

Fig. 11. Results of using the DT-ℂWT and Farnebäck algorithms to estimate a projective distortion to an image. Top left: the original, undistorted image with the region of interest (ROI) over which motion vectors were estimated highlighted. Top right: percentage pixel errors in the ROI of the distorted image. Lower left: percentage pixel errors in the ROI of the image corrected using the DT-ℂWT algorithm. Lower right: percentage pixel errors in the ROI of the image corrected using the Farnebäck algorithm.

the DT-ℂWT or Farnebäck algorithms in particular as being superior for use with SO_2 camera images. That said, the results produced by both when applied to the Villarrica and ATHAM datasets were encouraging, and suggest that, even if not optimal, either algorithm would be a reasonable choice for this application. For real-time processing applications however, the Farnebäck algorithm is more suitable than the DT-ℂWT algorithm as it is ~6 times faster. Using a PC with a 2.8 GHz Intel Core i5 processor the Farnebäck algorithm required 1.1 s to compute the motion vectors between a pair of 1024 × 1024 pixel images, whereas the DT-ℂWT algorithm took 6.1 s. The computation time for both algorithms scales linearly with the number of pixels in the images, meaning that large performance increases can be achieved by reducing the size of the images prior to motion estimation. Recent releases of the OpenCV library (Bradski, 2000) include an implementation of the Farnebäck algorithm which utilises the large-scale parallelism of modern graphics cards to increase the speed of the algorithm. In tests using a NVIDIA GeForce GTX 680 M graphics card, we found this to reduce the computation time to 90 ms for a pair of 1024 × 1024 pixel images.

More specialised optical-flow algorithms exist, which are specifically designed for tracking fluid flows (e.g. (Nogawa et al., 1997; Corpetti et al., 2002)). As such, they incorporate constraints from fluid mechanics, such as continuity, to prevent un-physical flow estimations. The findings of (Corpetti et al., 2002) show that inclusion of these constraints can lead to improved accuracy of the motion estimates produced for fluid flows. Such algorithms may be more suitable for estimating the plume transport speed than the DT-ℂWT or Farnebäck algorithms. However, successful application of the continuity constraint relies on accurate knowledge of the SO_2 amounts in each pixel. Whilst this is the case for the synthetic images produced by ATHAM, the calibration of real images is subject to unquantifiable error values and it is not clear how these errors might propagate into the motion estimate. In the future it may be possible to combine the motion estimates and the apparent absorbance data into a single coherent plume model which could then be inverted for SO_2 flux taking into account continuity constraints and therefore minimising the errors from both the motion and the calibration. However, this is beyond the scope of this investigation.

Synthetic plume images, such as those created using ATHAM, are clearly a useful validation tool for SO_2 flux calculation techniques as they enable quantitative error calculations to be made. In addition to validation, they also facilitate analysis and tuning of motion estimation algorithms which is not otherwise possible. For example, the choice of input parameters for an algorithm could be optimised by systematically varying its input parameters, applying it to a synthetic image sequence, and minimising the mean-squared error with respect to the known velocities (e.g. using Levenberg–Marquardt optimisation (Levenberg, 1944; Marquardt, 1963)). However, it is worth keeping in mind that a choice of parameters that can perfectly reproduce the velocity field of the synthetic images will not necessarily work well when applied to real data. This is of course dependent on how representative the modelled data are of real plumes.

The sensitivity of the two algorithms to their input parameters largely depends on the images being analysed. For images containing a lot of structure in the plume that does not move significantly between frames

(i.e. high frame-rate), both algorithms could be described as having a "linear" response to their input parameters (i.e. a small change in parameters will result in a small change in estimated motion). However, for images recorded at a lower frame-rate or that only have large scale structure in the plume, a high level of averaging must be used or the algorithms will fail to produce a physical result. Although both algorithms can be used successfully on low frame-rate data, the large amount of averaging required results in a very coarse motion estimate, and, in such situations the advantages over the cross-correlation technique may not be so significant.

The configuration and setup of the model used in this study was limited by computing time, and it is likely that with more resources its capabilities could be exploited to a greater extent. In particular, our simulations fail to reproduce the very rapid dilution of the plume that is seen in the Villarrica images. This may be due in part to the fact that the model is run only in two-dimensions, greatly reducing the scope for entrainment of the surrounding atmosphere into the plume. A three-dimensional setup using ATHAM, whilst possible, would be extremely computationally expensive. It would, however, facilitate very useful studies into the effects of treating a real volcanic plume as a two-dimensional object when calculating transport speeds. It is important to remember that each pixel in a SO_2 camera image represents an integrated amount of SO_2 in the plume along the optical path of that pixel. Hence, estimating motion vectors from such an image can only ever yield a coarse approximation to the true plume velocity. Three-dimensional plume model data would allow the errors introduced by estimating transport speeds from a two-dimensional projection of the plume to be constrained.

Although both algorithms were able to accurately compute the transformation required to correct our distorted image, in reality the problem is more complex. The image pairs to be registered from SO_2 camera systems employing two camera units are captured at different wavebands and features visible in one image may not be present in the other. This will likely degrade the performance of the algorithms and may compromise their ability to compute the motion vectors altogether. The extent of this problem will depend on the composition of the specific plume being imaged, and could be alleviated by careful selection of regions of the images over which to perform the motion estimation. An alternative approach would be to periodically capture a set of images at the same waveband from both cameras and use these to compute the registration parameters required.

It is theoretically possible to use the motion estimation techniques to correct for more complex image distortions than the projective transformation which we demonstrated (e.g. radial lens distortions). However, allowing more degrees of freedom when calculating the corrective transformation will lead to a less robust result, which is more susceptible to errors in the motion estimates. Since the lens distortion should be relatively constant, we believe that this correction would be better calculated prior to field deployment of the camera, perhaps using the well-established "chess board" technique (described in detail by (Bradski and Kaehler, 2008)).

5. Conclusions

We have presented two different motion estimation algorithms, a DT-ℂWT based algorithm and the Farnebäck algorithm, and showed how they can be applied to SO_2 camera images to improve the calculation of SO_2 flux. The ATHAM model was used to create a set of synthetic SO_2 camera images for which the SO_2 amounts and velocity field were known, and these were used to validate the estimates produced by the two algorithms.

Motion estimation algorithms are clearly a useful tool when applied to flux measurements using SO_2 cameras. It has been found in this study that they can provide a means to accurately register images from two separate camera units, in addition to providing more robust estimates of plume velocity for use in flux calculations than the currently-used cross-correlation method. The two algorithms presented here were similar in performance and would both be suitable for SO_2 camera applications, however, the Farnebäck algorithm is considerably faster, making it a better choice for real-time processing. A more thorough comparison of different algorithms is needed to determine the optimal algorithm for SO_2 camera applications.

Using plume models, such as ATHAM, to produce test datasets for motion estimation algorithms provides a simple way to evaluate and compare their performance. Further research is required to ensure that the data produced are an accurate representation of real volcanic plumes, and extension of the model setup into three-dimensions promises to provide valuable insights into the errors associated with flux measurements.

Supplementary data to this article can be found online at http://dx.doi.org/10.1016/j.jvolgeores.2014.08.031.

Acknowledgments

This work was supported by the UK National Centre for Earth Observation "Dynamic Earth and Geohazards" theme (NERC NE/F001487/1: http://comet.nerc.ac.uk/). The Villarrica dataset was collected with help from Kelby Hicks, Yves Moussallam, Kayla Iacovino and Tehnuka Ilanko during fieldwork supported by the Royal Geographical Society (with IBG) with a Geographical Fieldwork Grant. Additional financial support for the fieldwork was given by Antofagasta plc via the University of Cambridge Centre for Latin American Studies. We are extremely grateful to Fernando Gil Cruz and OVDAS for their logistical support and help in the field. We also thank Nick Kingsbury for providing the implementation of the DT-ℂWT algorithm. We are grateful to the two anonymous referees of the manuscript for their beneficial comments.

Appendix A. Algorithm parameters

The following sections describe the input parameters for the two motion estimation algorithms, and list the values that were assigned to them for this investigation. We refer to the parameters by the same names as are used in the source-code and documentation for the specific implementations that we used (see Section 2.1). Optional parameters that have not been defined below were left set to their default values. Different values were used for the image registration (Fig. 11) and the plume speed estimations (Figs. 2, 4 and 8). Both sets of values are listed in the tables below.

Appendix A.1. DT-ℂWT algorithm

Table A.1
Parameters used with DT-ℂWT algorithm for both image registration and plume speed estimation.

Parameter	Value for flux estimation	Value for registration
w	[−π/2.15, − 3π/2.15]	[−π/2.15, − 3π/2.15]
nit	6	6
levelsel	[[6, 4], [6, 3], [5, 3], [5, 3]]	[[4, 4], [4, 3], [4, 3], [4, 3], [4, 2]]
sizeqfilt	[4, 2, 2, 1]	[48, 32, 32, 16]
avlevel	3	4

w — Expected phase rotation per sample of the high and low band filters used in the DT-ℂWT decomposition.
nit — Number of iterations of the algorithm. A higher value may lead to a more refined motion estimate, but at the expense of increased computation time.
levelsel — Defines the coarsest and finest ℂ WT levels to be used during each iteration. In general it is best to use only the coarse levels for the early iterations, and then gradually expand the range to progressively finer levels. This parameter effectively selects the "size" of the features that are being tracked. Use of larger features often gives estimates that are less prone to noise, but also results in a less detailed velocity field.
sizeqfilt — Defines the size of the smoothing filter used at each iteration. A larger filter gives a smoother velocity field, but also causes loss of detail.
avlevel — Defines the ℂ WT level which has the same resolution as the velocity estimates.

Appendix A.2. Farnebäck algorithm

Table A.2
Parameters used with Farnebäck algorithm for both image registration and plume speed estimation.

Parameter	Value for flux estimation	Value for registration
pyr_scale	0.5	0.5
levels	4	3
winsize	20	15
iterations	5	10
poly_n	7	5
poly_sigma	1.5	1.2
flags	OPTFLOW_FARNEBACK_ GAUSSIAN	OPTFLOW_FARNEBACK_ GAUSSIAN

pyr_scale — Scale factor for each pyramid level compared to the previous.
levels — Number of pyramid levels to create. A higher number results in coarser features being used for the initial motion estimate.
winsize — Defines the size of the averaging filter used. A larger filter gives a smoother velocity field, but also causes loss of detail.
iterations — Defines the number of iterations of the algorithm at each pyramid level. A higher value may lead to a more refined motion estimate, but at the expense of increased computation time.
poly_n — Size of the neighbourhood used in the polynomial expansion for each pixel. A higher value results in more robust, but less detailed motion estimates.
poly_sigma — The standard deviation of the Gaussian smoothing filter used during the polynomial expansion.
flags — Optional parameters. We used the OPTFLOW_FARNEBACK_GAUSSIAN option so that the algorithm uses a Gaussian filter rather than a simple "box" filter. This gives more robust motion estimates at the expense of increased computation time.

Appendix B. ATHAM configuration

For our validation exercise, we used the same volcano model configuration as previous volcanological studies using ATHAM (Herzog et al., 1998, 2003; Oberhuber et al., 1998). The volcanic topography was parametrised as a simple Gaussian-shaped mountain with a height of 2850 m and a width parameter chosen such that the height-to-base ratio (500/2000) captured within our model domain roughly matched that of the Villarrica edifice. The crater was also chosen to be Gaussian-shaped (inverted), with a depth of 100 m, a width parameter of 50 m, and a flat bottom. Emissions from Villarrica typically emanate from large (5–20 m) vents in the cooled-crust covering the ~40 m-diameter lava lake that occupies the base of its crater (Witter et al., 2004; Shinohara and Witter, 2005). To emulate heat and volcanic gas fluxes from the lake, we applied a vertical velocity forcing over the cross-section of a lake, assumed to have a 50 m diameter. The baseline "exit" velocity was prescribed at 1 ms^{-1}, ramped up over 30 s, then modulated in time by a sine function of the same amplitude and a period of 2 min, mimicking periodicity in lake activity. Additionally, we superimposed random heterogeneity at each of the lake's 25 grid-points of $\pm 50\%$ of the "exit" velocity. The potential temperature of the erupting gas-particle mixture above the lake was set to 1000 K, and specific gas and aerosol concentrations were aligned with the values measured by Sawyer et al. (2011). From the tabled mass ratios of emitted gas species (Sawyer et al., 2011), we set the specific concentrations of the two gaseous tracers included in our model runs, magmatic H_2O and SO_2, to 782 and 79 g kg^{-1}, respectively. From the ratio of the measured mass fluxes of SO_2 (3.7 kg s^{-1}) to aerosol (1 kg s^{-1}), we inferred a total aerosol active tracer specific concentration of 21 g kg^{-1}. The remainder was assumed to be dry air from unresolved near-surface turbulent entrainment. All particulate aerosol was assigned to a single size bin with a radius of 0.5 μm and in equal amounts of 7 g kg^{-1} to 3 size bins with radii of 0.1, 0.5 and 5 μm in a second simulation as described in Section 3. All aerosol was given a specific heat capacity of 1200 J $kg^{-1}K^{-1}$ and a density of 2000 kg m^{-3}. Note that the actual values chosen to characterise volcanic degassing are not overly important, as the primary objective of the modelling exercise is to provide validation for motion estimation algorithms, rather than to constrain accurate plume dynamics and composition of a specific volcano. The turbulent length scale, and the horizontal and vertical TKE components over the lake were set to 2 m and 2 m^2s^2, respectively.

To account for wind-driven advection, without incurring excessive computational expense, we opted for a two-dimensional Cartesian grid, acknowledging that this approach precludes three-dimensional turbulent entrainment and therefore limits effective plume dispersion. An equal and homogeneous grid-spacing of 2 m in both the horizontal and vertical dimensions was used, roughly matching the 1 m^2 pixel size of our Villarrica dataset (Section 2.3). We used 1010 × 751 grid-points to cover a domain 2018 m wide and 1500 m high, starting at an altitude of 2350 m. A no-slip condition was applied at the ground-level lower boundary, characterised by a roughness length of 10 cm; the lateral boundaries were open. The top boundary was treated as a rigid lid. Open boundaries defy mass conservation within the domain, requiring us to limit our simulations to 15 min. The minimum and maximum time steps were 0.01 and 1 s, respectively, and the variable time step is governed by a Courant–Friederichs–Lewy criterion (Courant et al., 1967) limited to 0.8 for advection. Complete model data-fields were output every minute, and the full velocity, density of the mixture and SO_2 specific concentration fields were output roughly every second. Typical runtime on two computational cores was approximately one week.

Atmospheric initial conditions are specified in the model via a standard single vertical sounding profile of temperature, relative humidity and horizontal winds. These characterise atmospheric stability and determine potential advective transport. We used a sounding from Puerto Montt (station SCTE/85799, 41.43° S 73.10° W; ~250 km south of Villarrica) collected on 8 February 2012, at 12:00 UTC (−4 h time zone), which sets the simulation start to 08:00:00 LT (local time). Since the crater extends out of the atmospheric boundary layer and into the free troposphere, we estimate that the use of an early morning profile is inconsequential to the evolution of the plume. Only the west–east (u) component of the horizontal wind was retained. This was aligned with the model's orientation, and scaled down to 20% of the measured values, in order to avoid excessively fast advection of the plume (and of turbulence) out of our small model domain, and strong up- and down-slope flow.

References

Bluth, G., Shannon, J., Watson, I., Prata, A., Realmuto, V., 2007. Development of an ultra-violet digital camera for volcanic SO_2 imaging. J. Volcanol. Geotherm. Res. 161, 47–56. http://dx.doi.org/10.1016/j.jvolgeores.2006.11.004 (http://www.sciencedirect.com/science/article/pii/S0377027306003957).

Boichu, M., Oppenheimer, C., Tsanev, V., Kyle, P.R., 2010. High temporal resolution SO_2 flux measurements at Erebus volcano, Antarctica. J. Volcanol. Geotherm. Res. 190, 325336. http://dx.doi.org/10.1016/j.jvolgeores.2009.11.020 (http://www.sciencedirect.com/science/article/B6VCS-4XVK3X7-2/2/5becf55734379e128652e28c05da2702).

Bradski, G., 2000. The OpenCV Library. Dr. Dobb's J. Softw. Tools 25, 122125 (120, URL: http://www.ddj.com/ftp/2000/2000_11/opencv.txt).

Bradski, G., Kaehler, A., 2008. Learning OpenCV: computer vision with the OpenCV Library, 1st ed. O'Reilly Media.

Campion, R., Martinez-Cruz, M., Lecocq, T., Caudron, C., Pacheco, J., Pinardi, G., Hermans, C., Carn, S., Bernard, A., 2012. Space- and ground-based measurements of sulphur dioxide emissions from Turrialba Volcano (Costa Rica). Bull. Volcanol. 74, 1757–1770. http://dx.doi.org/10.1007/s00445-012-0631-z (http://www.springerlink.com/index/10.1007/s00445-012-0631-z).

Corpetti, T., Memin, E., Perez, P., 2002. Dense estimation of fluid flows. IEEE Trans. Pattern Anal. Mach. Intell. 24, 365–380. http://dx.doi.org/10.1109/34.990137.

Courant, R., Friedrichs, K., Lewy, H., 1967. On the partial difference equations of mathematical physics. IBM J. Res. Dev. 11, 215–234. http://dx.doi.org/10.1147/rd.112.0215.

Dalton, M.P., Watson, I.M., Nadeau, P.A., Werner, C., Morrow, W., Shannon, J.M., 2009. Assessment of the UV camera sulfur dioxide retrieval for point source plumes. J. Volcanol. Geotherm. Res. 188, 358–366. http://dx.doi.org/10.1016/j.jvolgeores.2009.09.013 (http://www.sciencedirect.com/science/article/pii/S0377027309003655).

Farnebäck, G., 2003. Two-frame motion estimation based on polynomial expansion. In: Bigun, J., Gustavsson, T. (Eds.), Image Analysisnumber 2749 in Lecture Notes in Computer Science. Springer Berlin Heidelberg, pp. 363–370 (http://link.springer.com/chapter/10.1007/3-540-45103-X_50).

Geiger, A., Lenz, P., Stiller, C., Urtasun, R., 2014. The KITTI vision benchmark suite, (http://www.cvlibs.net/datasets/kitti/eval_stereo_flow.php?benchmark=flow).

Herzog, M., Graf, H.F., 2010. Applying the three-dimensional model ATHAM to volcanic plumes: dynamic of large co-ignimbrite eruptions and associated injection heights

for volcanic gases. Geophys. Res. Lett. 37, L19807. http://dx.doi.org/10.1029/2010GL044986 (http://onlinelibrary.wiley.com/doi/10.1029/2010GL044986/abstract).
Herzog, M., Graf, H.F., Textor, C., Oberhuber, J.M., 1998. The effect of phase changes of water on the development of volcanic plumes. J. Volcanol. Geotherm. Res. 87, 55–74. http://dx.doi.org/10.1016/S0377-0273(98)00100-0 (http://www.sciencedirect.com/science/article/pii/S0377027398001000).
Herzog, M., Oberhuber, J.M., Graf, H.F., 2003. A prognostic turbulence scheme for the nonhydrostatic plume model ATHAM. J. Atmos. Sci. 60, 2783–2796.
Holland, A.P., Watson, I.M., Phillips, J.C., Caricchi, L., Dalton, M.P., 2011. Degassing processes during lava dome growth: insights from Santiaguito lava dome, Guatemala. J. Volcanol. Geotherm. Res. 202, 153–166. http://dx.doi.org/10.1016/j.jvolgeores.2011.02.004 (http://www.sciencedirect.com/science/article/pii/S0377027311000515).
James, M.R., Pinkerton, H., Robson, S., 2007. Image-based measurement of flux variation in distal regions of active lava flows. Geochem. Geophys. Geosyst. 8, Q03006. http://dx.doi.org/10.1029/2006GC001448 (http://onlinelibrary.wiley.com/doi/10.1029/2006GC001448/abstract).
Kantzas, E.P., McGonigle, A., Tamburello, G., Aiuppa, A., Bryant, R.G., 2010. Protocols for UV camera volcanic SO_2 measurements. J. Volcanol. Geotherm. Res. 194, 55–60. http://dx.doi.org/10.1016/j.jvolgeores.2010.05.003 (http://www.sciencedirect.com/science/article/pii/S0377027310001447).
Kern, C., Kick, F., Lübcke, P., Vogel, L., Whrbach, M., Platt, U., 2010. Theoretical description of functionality, applications, and limitations of SO_2 cameras for the remote sensing of volcanic plumes. Atmos. Meas. Tech. Discuss. 3, 531–578. http://dx.doi.org/10.5194/amtd-3-531-2010 (http://www.atmos-meas-tech-discuss.net/3/531/2010/amtd-3-531-2010.html).
Kern, C., Werner, C.A., Doukas, M.P., Elias, T., Kelly, P.J., Sutton, A.J., 2012. Imaging volcanic SO_2 plumes with UV cameras. EGU General Assembly Conference Abstracts, p. 12596 (http://adsabs.harvard.edu/abs/2012EGUGA..1412596K).
Kern, C., Werner, C., Elias, T., Sutton, A.J., Lübcke, P., 2013. Applying UV cameras for SO_2 detection to distant or optically thick volcanic plumes. J. Volcanol. Geotherm. Res. 262, 80–89. http://dx.doi.org/10.1016/j.jvolgeores.2013.06.009 (http://www.sciencedirect.com/science/article/pii/S0377027313001832).
Kingsbury, N., 2001. Complex wavelets for shift invariant analysis and filtering of signals. Appl. Comput. Harmon. Anal. 10, 234253. http://dx.doi.org/10.1006/acha.2000.0343 (http://www.sciencedirect.com/science/article/B6WB3-45BT4JT-X/2/e88b2a92c22b0e1ae0475e7399b0f45f).
La Spina, A., Salerno, G., Burton, M., 2013. Recent SO_2 camera and OP-FTIR field measurements in Mexico and Guatemala. EGU General Assembly Conference Abstracts, p. 10478 (http://adsabs.harvard.edu/abs/2013EGUGA..1510478L).
Lev, E., Spiegelman, M., Wysocki, R.J., Karson, J.A., 2012. Investigating lava flow rheology using video analysis and numerical flow models. J. Volcanol. Geotherm. Res. 247248, 62–73. http://dx.doi.org/10.1016/j.jvolgeores.2012.08.002 (http://www.sciencedirect.com/science/article/pii/S0377027312002405).
Levenberg, K., 1944. A method for the solution of certain non-linear problems in least-squares. Q. Appl. Math. 2, 164168.
Lübcke, P., Bobrowski, N., Illing, S., Kern, C., Alvarez Nieves, J.M., Vogel, L., Zielcke, J., Delgado Granados, H., Platt, U., 2012. On the absolute calibration of SO_2 cameras. Atmos. Meas. Tech. Discuss. 5, 6183–6240. http://dx.doi.org/10.5194/amtd-5-6183-2012 (http://www.atmos-meas-tech-discuss.net/5/6183/2012/).
Magarey, J., Kingsbury, N., 1998. Motion estimation using a complex-valued wavelet transform. Signal Process. IEEE Trans. 46, 10691084. http://dx.doi.org/10.1109/78.668557.
Marquardt, D.W., 1963. An algorithm for the least-squares estimation of nonlinear parameters. SIAM J. Appl. Math. 11, 431441.
Mather, T., Allen, A., Davison, B., Pyle, D., Oppenheimer, C., McGonigle, A., 2004a. Nitric acid from volcanoes. Earth Planet. Sci. Lett. 218, 17–30. http://dx.doi.org/10.1016/S0012-821X(03)00640-X (http://www.sciencedirect.com/science/article/pii/S0012821X0300640X).
Mather, T.A., Tsanev, V.I., Pyle, D.M., McGonigle, A.J.S., Oppenheimer, C., Allen, A.G., 2004b. Characterization and evolution of tropospheric plumes from Lascar and Villarrica volcanoes, Chile. J. Geophys. Res. Atmos. 109. http://dx.doi.org/10.1029/2004JD004934 (http://onlinelibrary.wiley.com/doi/10.1029/2004JD004934/abstract).
McGonigle, A.J.S., Hilton, D.R., Fischer, T.P., Oppenheimer, C., 2005a. Plume velocity determination for volcanic SO_2 flux measurements. Geophys. Res. Lett. 32, L11302. http://dx.doi.org/10.1029/2005GL022470 (http://onlinelibrary.wiley.com/doi/10.1029/2005GL022470/abstract).
McGonigle, A.J.S., Inguaggiato, S., Aiuppa, A., Hayes, A.R., Oppenheimer, C., 2005b. Accurate measurement of volcanic SO_2 flux: determination of plume transport speed and integrated SO_2 concentration with a single device. Geochem. Geophys. Geosyst. 6. http://dx.doi.org/10.1029/2004GC000845 (http://onlinelibrary.wiley.com/doi/10.1029/2004GC000845/abstract).
Mori, T., Burton, M., 2006. The SO_2 camera: a simple, fast and cheap method for ground-based imaging of SO_2 in volcanic plumes. Geophys. Res. Lett. 33, L24804. http://dx.doi.org/10.1029/2006GL027916 (http://www.agu.org/pubs/crossref/2006/2006GL027916.shtml).
Mori, T., Burton, M., 2009. Quantification of the gas mass emitted during single explosions on Stromboli with the SO_2 imaging camera. J. Volcanol. Geotherm. Res. 188, 395–400. http://dx.doi.org/10.1016/j.jvolgeores.2009.10.005 (http://www.sciencedirect.com/science/article/pii/S0377027309003990).
Nogawa, H., Nakajima, Y., Sato, Y., Tamura, S., 1997. Acquisition of symbolic description from flow fields: a new approach based on a fluid model. IEEE Trans. Pattern Anal. Mach. Intell. 19, 58–63. http://dx.doi.org/10.1109/34.566811.
Oberhuber, J.M., Herzog, M., Graf, H.F., Schwanke, K., 1998. Volcanic plume simulation on large scales. J. Volcanol. Geotherm. Res. 87, 29–53. http://dx.doi.org/10.1016/S0377-0273(98)00099-7 (http://www.sciencedirect.com/science/article/pii/S0377027398000997).
Oppenheimer, C., Lomakina, A.S., Kyle, P.R., Kingsbury, N.G., Boichu, M., 2009. Pulsatory magma supply to a phonolite lava lake. Earth Planet. Sci. Lett. 284, 392398. http://dx.doi.org/10.1016/j.epsl.2009.04.043 (http://www.sciencedirect.com/science/article/B6V61-4WH0JVH-1/2/9bfe0fa47d44d452b045397b50b40d01).
Pering, T.D., Tamburello, G., McGonigle, A.J.S., Aiuppa, A., Cannata, A., Giudice, G., Patan, D., 2014. High time resolution fluctuations in volcanic carbon dioxide degassing from Mount Etna. J. Volcanol. Geotherm. Res. 270, 115–121. http://dx.doi.org/10.1016/j.jvolgeores.2013.11.014 (http://www.sciencedirect.com/science/article/pii/S0377027313003508).
Peters, N., Oppenheimer, C., Kyle, P., Kingsbury, N., 2014a. Decadal persistence of cycles in lava lake motion at Erebus volcano, Antarctica. Earth Planet. Sci. Lett. 395, 1–12. http://dx.doi.org/10.1016/j.epsl.2014.03.032 (http://www.sciencedirect.com/science/article/pii/S0012821X14001848).
Peters, N., Oppenheimer, C., Killingsworth, D.R., Frechette, J., Kyle, P., 2014b. Correlation of cycles in lava lake motion and degassing at Erebus Volcano, Antarctica. Geochem. Geophys. Geosyst. 15, 3244–3257.
Sawyer, G., Salerno, G., Le Blond, J., Martin, R., Spampinato, L., Roberts, T., Mather, T., Witt, M., Tsanev, V., Oppenheimer, C., 2011. Gas and aerosol emissions from Villarrica volcano, Chile. J. Volcanol. Geotherm. Res. 203, 62–75. http://dx.doi.org/10.1016/j.jvolgeores.2011.04.003 (http://www.sciencedirect.com/science/article/pii/S0377027311000850).
Shinohara, H., Witter, J.B., 2005. Volcanic gases emitted during mild Strombolian activity of Villarrica volcano, Chile. Geophys. Res. Lett. 32. http://dx.doi.org/10.1029/2005GL024131 (http://onlinelibrary.wiley.com/doi/10.1029/2005GL024131/abstract).
Smekens, J., Burton, M.R., Clarke, A.B., Harijoko, A., Wibowo, H., Sawyer, G., 2013. High frequency SO_2 flux measurements at Semeru volcano, Indonesia, using the SO_2 camera. AGU Fall Meet. Abstr. 1, 2882 (http://adsabs.harvard.edu/abs/2013AGUFM.V43B2882S).
Tamburello, G., Kantzas, E., McGonigle, A., Aiuppa, A., Giudice, G., 2011. UV camera measurements of fumarole field degassing (La Fossa crater, Vulcano Island). J. Volcanol. Geotherm. Res. 199, 47–52. http://dx.doi.org/10.1016/j.jvolgeores.2010.10.004 (http://www.sciencedirect.com/science/article/pii/S0377027310003148).
Tamburello, G., Aiuppa, A., Kantzas, E., McGonigle, A., Ripepe, M., 2012. Passive vs. active degassing modes at an open-vent volcano (Stromboli, Italy). Earth Planet. Sci. Lett. 106–116 http://dx.doi.org/10.1016/j.epsl.2012.09.050 (http://www.sciencedirect.com/science/article/pii/S0012821X12005468).
Tamburello, G., Aiuppa, A., McGonigle, A.J.S., Allard, P., Cannata, A., Giudice, G., Kantzas, E.P., Pering, T.D., 2013. Periodic volcanic degassing behavior: the Mount Etna example. Geophys. Res. Lett. 40, 48184822. http://dx.doi.org/10.1002/grl.50924 (http://onlinelibrary.wiley.com/doi/10.1002/grl.50924/abstract).
Textor, C., Graf, H.F., Herzog, M., Oberhuber, J.M., Rose, W.I., Ernst, G.G.J., 2006a. Volcanic particle aggregation in explosive eruption columns. Part I: parameterization of the microphysics of hydrometeors and ash. J. Volcanol. Geotherm. Res. 150, 359–377. http://dx.doi.org/10.1016/j.jvolgeores.2005.09.007 (http://www.sciencedirect.com/science/article/pii/S0377027305002982).
Textor, C., Graf, H.F., Herzog, M., Oberhuber, J.M., Rose, W.I., Ernst, G.G.J., 2006b. Volcanic particle aggregation in explosive eruption columns. Part II: numerical experiments. J. Volcanol. Geotherm. Res. 150, 378–394. http://dx.doi.org/10.1016/j.jvolgeores.2005.09.008 (http://www.sciencedirect.com/science/article/pii/S0377027305002994).
Van Eaton, A.R., Herzog, M., Wilson, C.J.N., McGregor, J., 2012. Ascent dynamics of large phreatomagmatic eruption clouds: the role of microphysics. J. Geophys. Res. Solid Earth 117, B03203. http://dx.doi.org/10.1029/2011JB008892 (http://onlinelibrary.wiley.com/doi/10.1029/2011JB008892/abstract).
Williams-Jones, G., Horton, K.A., Elias, T., Garbeil, H., Mouginis-Mark, P.J., Sutton, A.J., Harris, A.J.L., 2006. Accurately measuring volcanic plume velocity with multiple UV spectrometers. Bull. Volcanol. 68, 328–332. http://dx.doi.org/10.1007/s00445-005-0013-x (http://link.springer.com/article/10.1007/s00445-005-0013-x).
Witter, J.B., Kress, V.C., Delmelle, P., Stix, J., 2004. Volatile degassing, petrology, and magma dynamics of the Villarrica Lava Lake, Southern Chile. J. Volcanol. Geotherm. Res. 134, 303–337. http://dx.doi.org/10.1016/j.jvolgeores.2004.03.002 (http://www.sciencedirect.com/science/article/pii/S0377027304000630).